Effect of stress-states on non-classical twinning in three-point bending of Magnesium alloys

Chaitanya Paramatmuni [1*], Fionn P.E. Dunne

Department of Materials, Imperial College London, London, SW7 2AZ, United Kingdom

Abstract

The influence of stress state on the drivers of non-classical twin nucleation in three-point bending of Magnesium alloy AZ31 is presented in this study. Deformed microstructures and textures at the tensile and, for the first time, shear regions are investigated in detail. The experimental observations coupled with the strain-gradient crystal plasticity analyses show that the shear nucleates more twins compared to the tensile and compressive stress-states at near yield-point. Stored energy density provides mechanistic insight into the local drivers of non-classical twin nucleation observed in the shear stress-state region. Further, the twin variant selection follows the locally stored shear energy density criterion, as opposed to the twin resolved shear stress, indicating that their nucleation is driven by local energy and defect sources.

Keywords

Three-point bending; Twin nucleation; Stress states; Stored energy density; Variant selection; Crystal plasticity.

[1] Currently at Department of Materials Science and Engineering, University of Sheffield, Sheffield, S1 3JD, United Kingdom

*Corresponding author
Email address: c.paramatmuni@sheffield.ac.uk

1. Introduction

The utilization of magnesium (Mg) alloys in automotive closure and cell phone body applications is gaining traction to achieve light-weighting without compromising on the required strength-to-weight ratio [1]. This desired formability is often achieved by performing the stamping processes at elevated temperatures [2, 3, 4]. However, the current need to optimize energy consumption is driving the research and development of the cold stamping processes [5, 6]. One of the several ways to understand the deformation caused by complex stress-states in a cold stamping process is by performing three/four-point bending of Mg alloys.

The bending process produces tensile, compressive and shear stress-states simultaneously within the sample. These stress-states and, therefore, the micromechanics are influenced by several factors such as the tension-compression asymmetry [7], surface features [8], texture (e.g. [9]) etc. The texture is reported to influence the bending behaviour of Mg alloys in several ways. It is demonstrated to affect the direction of shift in neutral axis during bending, which is caused by the type of deformation modes activated within the material [10, 11]. Similarly, it is also shown in other studies that the texture drives the preferential formation of extension twins and subsequent texture evolution during bending [12, 13, 14, 15].

Similarly, Liu et al. [16] and Tang et al. [15] studied the effect of strong and weak starting textures on deformation behaviour of Mg alloys during bending. While the former suggested that the observed twinning was driven by local slip, it appears in the latter that twins were driven by local stresses. Paramatmuni et al. [17] defined the twins that are driven by the local energy and defect sources as non-classical, where the local shear stored energy determines the variant selection. It was demonstrated that these twins, which are also referred as non-Schmid twins, occur within parent grains that possess unfavourable local twin-resolved shear stresses (TRSS). In contrast, the twins that are driven by local favourable stresses are termed as classical twins, which are often called Schmid twins that possess positive global Schmid factors and/or

appropriately high local TRSSs. The majority of experimental studies that investigated the micromechanics of Mg alloy twinning during three-point bending reported the formation of only classical twins [16]. Further, for a given texture, the deformation behaviour of Mg alloys depends on the evolution of local incompatibilities driven by the microstructure. For instance, Baird et al. [18] reported the formation of twins in only the compressive region of rolled Mg alloy AZ31 during bending, while McClelland et al. [19] showed twins also in the tensile region, where the c-axes of grains are almost perpendicular to the local tensile stress component. They argued that these twins with very low Schmid factors were driven by the local strain incompatibilities.

These studies provide unequivocal evidence for the complex deformation behaviour of Mg alloys in bending. However, the texture in the majority of these studies is such that the bending stress renders favourable conditions for the activation of twinning in tensile or compressive regions. To the authors' knowledge, there are limited studies such as [16] and [15] that studied the effect of bending stress normal to the ND (e.g. Bending-ND case in [15]). While the former investigated the twinning formation and texture evolution within a friction stir welded Mg alloy AZ31, the latter studied the heterogeneous deformation behaviour of an extruded Mg alloy AZ31. However, as the Mg alloys in the sheet form are often subjected to stamping operations, it is necessary to understand the response of the rolled alloy during bending when loaded along the ND.

Studies focused on the tensile and compressive regions of samples have not investigated the influence of shear stress-state on twin formation. However, Huang et al. [20] studied the effect of local shear strain on twin formation. The qualitative observation of their microstructures indicate that the high localized shear strain nucleates more twins when compared with that of low shear strain. Thus, in addition to compressive and tensile, it is necessary to study the shear regions of the bending sample to obtain more complete understanding of twin formation and

resulting texture evolution during three-point bending. While the formation of twins has been shown to improve the bending formability of Mg alloys [21, 22, 23, 24], other studies suggest that their formation inhibits the performance (e.g. [14]). Therefore, it is necessary to identify the type of stress-states for a given starting texture that favour their formation to tailor the Mg alloy components based on the application.

Thus, in the current study rolled Mg alloy AZ31 is subjected to three-point bending generating both in-plane shear and bending stresses normal to the ND to investigate the effect of stress-state on non-classical twin formation, variant selection and texture evolution. In addition, the micromechanical drivers of non-classical twin nucleation, the preferred microstructural locations, and the variants selected are investigated experimentally. The observations are then assessed with finite element strain-gradient crystal plasticity (CPFE) modelling to understand the mechanistic drivers of non-classical twin nucleation and variant selection and their dependence on macroscale stress state. The article is structured as follows: the following section details the experimental and computational methods employed in the current study. Section 3 presents the experimental results of undeformed and deformed samples and the crystal plasticity analyses. These results are then discussed in section 4, and the findings of this work are summarized in section 5.

2. Methods

The material preparation, characterisation of samples before and after deformation, and the three-point bending methods are detailed in the first part of this section. Later, the CPFE framework including the stored energy density and the shear stored energy density criteria, which provide the drivers of twin nucleation and variant selection respectively, are briefly introduced.

2.1 Mechanical testing and material characterization

The Mg alloy AZ31, as detailed in [25], was received in the warm-rolled condition with a thickness of 7 mm. The as-received material was annealed at 350 °C for 2 hours to obtain a twin-free microstructure. Then, the three-point bending specimen with dimensions of 4x3x12 mm^3 was extracted using the electrical discharge machine (wire-EDM). The experimental set-up in a Shimadzu universal testing machine [26] was used to perform three-point bending at the strain rate of 0.001 1/s until a macroscopic displacement of 2 mm.

The microstructures before and after deformation were characterized by performing electron back-scatter diffraction (EBSD). The samples were initially prepared by following standard metallography procedures until the 4000 grit size. Then, they were fine polished using colloidal silica. The samples were then cleaned using methanol to remove the remnant colloidal silica on the surface. Finally, they were ion-polished in a GATAN-PECS-II machine by following the steps described in [25]. The EBSD was performed in a ZEISS Sigma 300 SEM equipped with a Bruker high resolution EBSD detector with the voltage of 20 kV and ~13 mm working distance. In order to understand the twin formation during three-point bending, areas of size ~500 x 500 μm^2 were scanned on the surface of the sample. The scanned data was then analysed using MTEX [27, 28], an open source MATLAB tool, to study the twin characteristics.

2.2 Computational framework

The CPFE framework developed in [29] and later implemented in Paramatmuni et al. [30] to understand twin nucleation is employed in this study. A brief description of the formulation is as follows:

The total deformation ($\mathbf{F}$) decomposed into plastic ($\mathbf{F}^p$) and elastic distortion and rigid body rotation ($\mathbf{F}^e$) is given as,

$$\mathbf{F} = \mathbf{F}^e\mathbf{F}^p \tag{1}$$

The plastic part in the above equation is a manifestation of local shear strain accommodated by crystallographic slip systems,

$$\mathbf{L}^{p} = \sum_{\alpha} \dot{\gamma}^{\alpha} \mathbf{s}^{\alpha} \otimes \mathbf{n}^{\alpha} \tag{2}$$

where $\mathbf{L}^{p}$ is the plastic velocity gradient, $\dot{\gamma}^{\alpha}$ the shear strain rate accommodated by a given slip system α, and $\mathbf{s}^{\alpha}$ and $\mathbf{n}^{\alpha}$ are the direction and plane normal of the slip system α.

The shear strain rate accommodated by the slip systems follows thermal activation of dislocations given as,

$$\dot{\gamma}^{\alpha} = \rho_{m} b^{\alpha 2} \nu_{D} \exp\left(-\frac{\Delta F}{kT}\right) \sinh\left(\frac{(\tau^{\alpha} - \tau_{c}^{\alpha})\Delta V^{\alpha}}{kT}\right) \tag{3}$$

where ρ_{m} is the mobile dislocation density, b^{α} is the Burger's vector magnitude of the slip system α, ν_{D} the Debye frequency, ΔF the activation energy, k the Boltzmann constant, τ^{α} and τ_{c}^{α} are the resolved and critical resolved shear stresses (CRSS) of the slip system α, and ΔV^{α} is the activation volume for the system α. The hardening of the slip systems is driven by the evolution of local dislocation densities [31] as,

$$\tau_{c}^{\alpha} = \tau_{0}^{\alpha} + \zeta^{\alpha} G b^{\alpha} \sqrt{\rho_{SSD} + \sum_{\alpha=1}^{n} \rho_{GND}^{\alpha}} \tag{4}$$

in which, for a given slip system α, τ_{0}^{α} indicates the initial slip resistance, ζ^{α} the hardening coefficient, G the shear modulus, and ρ_{SSD} and ρ_{GND} are the statistically stored (SSD) and geometrically necessary dislocation (GND) densities respectively. The evolution of the SSD density at a material point follows the plastic strain rate as,

$$\rho_{SSD} = \Gamma \int_{0}^{t} \dot{p}\, dt \tag{5}$$

where Γ determines the rate of density evolution and $\dot{p}$ is the plastic strain rate. The GND varies with the local strain gradients that accommodate lattice curvatures. This is formulated as a relationship between the Nye tensor and the GND [32] as,

$$\text{curl}\,(\mathbf{F}^{p}) = \sum_{\alpha=1}^{n} \mathbf{\Lambda}^{\alpha} \rho_{gnd}^{\alpha} \quad (6)$$

in which $\mathbf{\Lambda}^{\alpha}$ is the second order tensor that contains the geometric information of a given slip system α (see [33] for more details).

The nucleation of twins is preceded by the accumulation of local dislocations within the parent grains at the grain boundaries. The interaction between these dislocations or between the dislocations and grain boundaries increase the local stresses, which increase the local energy stored in the material in the form of dislocation structures. This local stored energy assists the disassociation of dislocation structures that lead to the formation of twin nuclei [34, 35]. Paramatmuni et al. [30] and Paramatmuni et al. [17] demonstrated that the stored energy density (G_{SE}) criterion satisfactorily captures microstructure-sensitive non-classical twin nucleation. Therefore, tracking the evolution of local stored energy allows precise identification of twin nucleation sites, and is employed in the current study to understand the effect of stress-states on twin formation during three-point bending. G_{SE} is defined as,

$$G_{SE} = \int \frac{\xi |\boldsymbol{\sigma} : d\boldsymbol{\varepsilon}^{p}|}{\sqrt{\rho_{SSD} + \sum_{\alpha=1}^{n} \rho_{GND}^{\alpha}}} \quad (7)$$

where ξ represents the fraction (5%) of energy stored within local dislocation structures due to plastic deformation [36]. As G_{SE} is stored preferentially by GNDs [36], a characteristic length scale is associated with this quantity. Further, Paramatmuni et al. [30] and Paramatmuni et al. [17] reported that the local G_{SE} should exceed a *critical* value of ~0.015 J/m^2 for non-classical twin nucleation.

One of six available variants of extension twins nucleate at a given material point [37]. In the case of classical twins, which are driven predominantly by local stresses, Paramatmuni et al. [17] reported that the twin resolved shear stress (TRSS) within the parent grain satisfactorily predicts the active twin variant. In contrast, the prediction of variant selection for non-classical

142 twins is complex and requires considering the effect of local incompatibilities which may be
143 driven by local dislocations and energy sources (e.g. [38, 39, 40]). Once G_{SE} attains the *critical*
144 value at a given parent grain boundary, the local dislocation structures disassociate to form
145 twin nucleus. That is, the type of active twin variant is decided at this incipient stage of twin
146 formation. Paramatmuni et al. [30] determined the energy density associated with the formation
147 of the nuclei of all six variants using their shear stored energy density (S_{SE}) criterion. As the
148 formation of a stable twin nuclei requires the total energy associated with the formation to be
149 minimum [41], Paramatmuni et al. [30] argued that the twin variant with the least S_{SE} is selected
150 within the parent grain. The S_{SE} is given as,

151 $$S_{SE} = \frac{\tau^{\beta}\,\gamma_{P}^{\beta}}{\sqrt{\rho_{SSD}+\sum_{\alpha=1}^{n}\rho_{GND}^{\alpha}}} \quad (8)$$

152 where τ^{β} is the shear stress and γ_{P}^{β} the accumulated shear strain resolved on plane $\mathbf{n^{\beta}}$ and along
153 direction $\mathbf{b^{\beta}}$ of twin variant β. The TRSS and the S_{SE} are both employed to predict variant
154 selection in the current study. Further, the elastic constants reported in [42] and the rate-
155 sensitive single crystal material parameters obtained in [25] are utilized in the current crystal
156 plasticity framework.

157 **3. Results**

158 The deformed and undeformed microstructures and textures are investigated in the first part of
159 this section. These experimental observations are employed with isotropic elasto-pastic three-
160 point bending analyses to identify the stress-states at different locations of the sample. In the
161 later part of this section, the effect of these stress-states is studied using the CPFE framework
162 to account for the microstructural heterogeneity. The CPFE results are investigated in detail to
163 understand the drivers of non-classical twin nucleation and variant selection.

164 **3.1 Experimental analyses of undeformed and deformed microstructures**

Fig. 1(a) shows the twin-free microstructure in the ND-TD plane before deformation. The microstructure shows the majority of c-axes of grains oriented along the ND (see section A), which is a characteristic of rolled Mg alloy AZ31. This implies that loading this microstructure generates bending stresses normal to the ND, which may render it unfavourable for the formation of extension twins. The schematic representation of the three-point bending

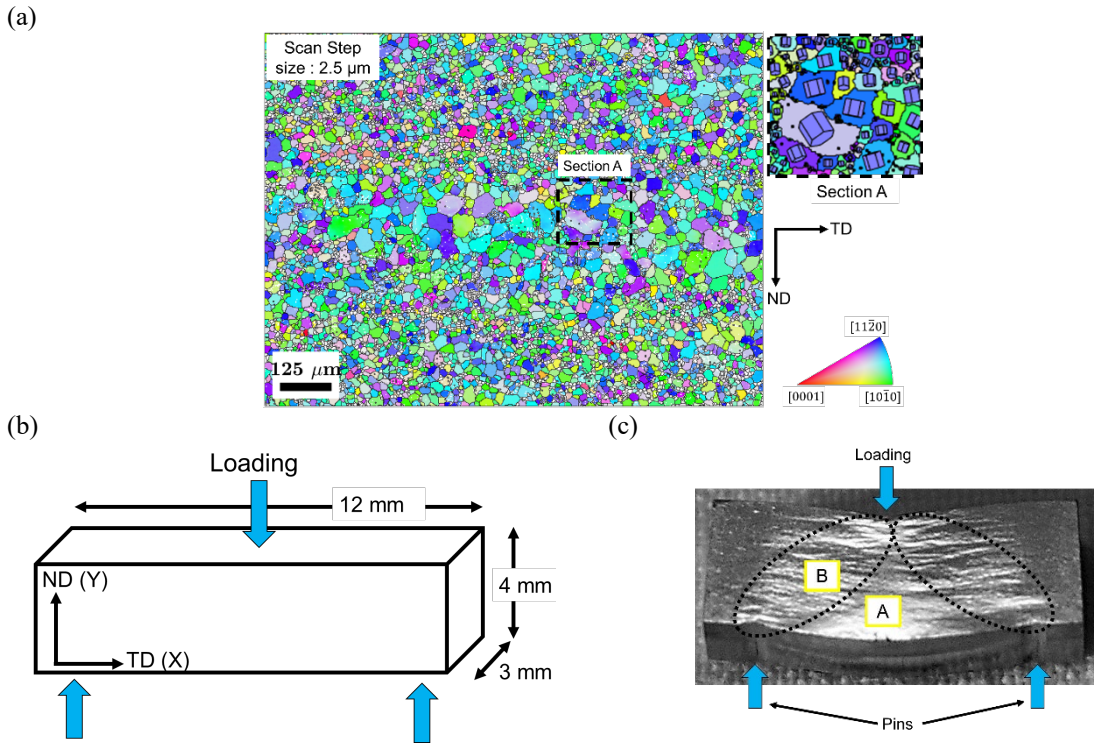

Fig. 1. The experimental set-up showing (a) IPF map of the undeformed microstructure of rolled Mg alloy AZ31with the insert indicating the texture with respect to bending stresses (normal to ND), (b) schematic representation of the three-point bending set-up and (c) the bent sample indicating the regions of interest A and B for further experimental and numerical analyses. The three-point bending resulted in symmetric deformation bands as shown in the figure. (For interpretation of the references to colour in this figure legend, the reader is referred to the Web version of this article.)

experimental set-up is shown in Fig. 1(b), indicating the loading direction, ND, TD and the sample dimensions. The figure shows that the macroscopic loading of the sample for three-point bending is along the TD, i.e. normal to the c-axes of the majority of grains. This implies that the The deformed sample after bending is shown in Fig. 1(c). The detailed examination of the sample surface shows two symmetric regions with deformation bands, while the rest of the sample remains relatively smooth. In order to understand the microstructures in these areas, two regions of interest (ROIs) A and B are picked to perform EBSD. The IPF maps and

corresponding basal pole figures of ROIs A and B are shown in Fig. 2. The microstructure at A (Fig. 2(a)) is similar to that of Fig. 1(a) with some intragranular misorientation indicating localized deformation. The corresponding texture in Fig. 2(b) shows strong basal texture with c-axes oriented along the ND, which may indicate that the local deformation is predominantly

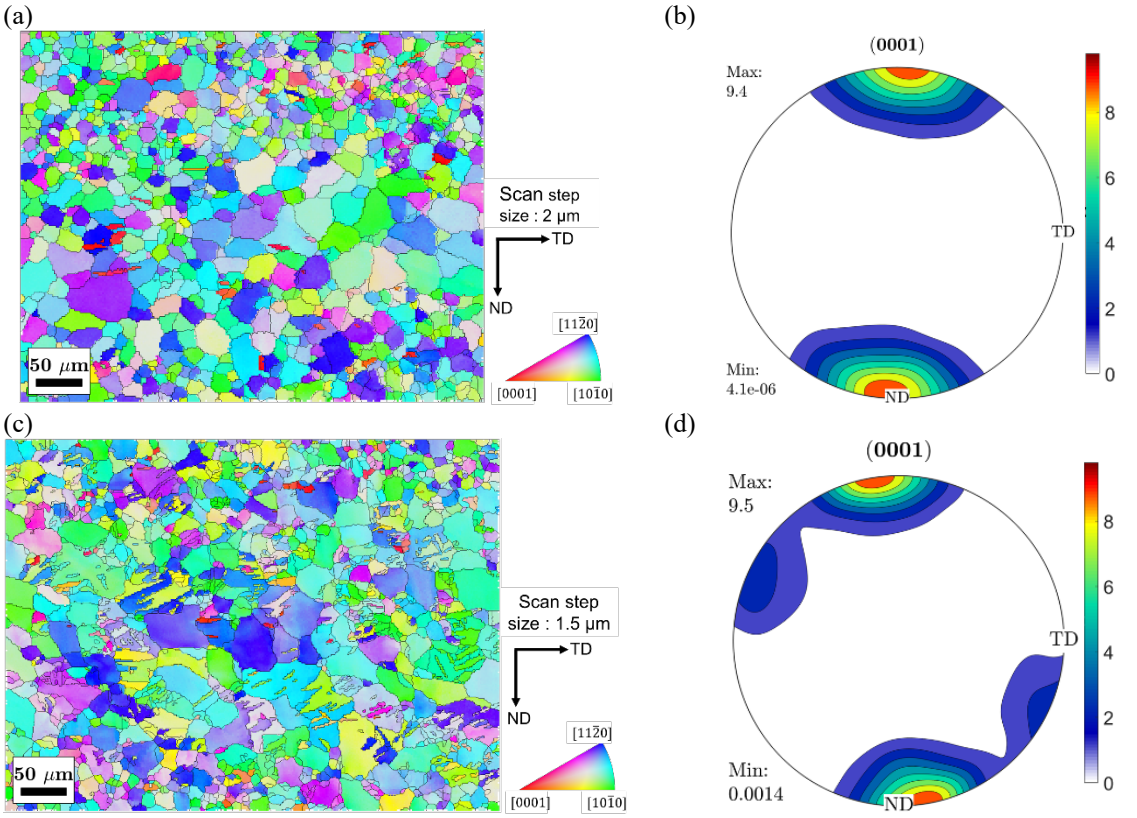

Fig. 2. The deformed microstructure and corresponding texture of the regions of interest in (a) and (b) ROI A, and (c) and (d) ROI B respectively. Observe features in IPF map of ROI B that are similar to extension twins and the texture reorientation in (d), which are absent in ROI A. (For interpretation of the references to colour in this figure legend, the reader is referred to the Web version of this article.)

accommodated by crystallographic slip. The deformed microstructure at location B (Fig. 2(c)) shows prominent intragranular misorientation along with the features that resemble extension twins. This is reflected in the corresponding basal pole figure (Fig. 2(d)), which shows the presence of orientations away from the ND. However, these orientations do not reflect the typically observed ~86.3 °reorientation of parent grains (e.g. [43]), which is a characteristic of extension twins. Therefore, the grain boundary misorientation angles within these microstructures are further investigated to confirm the formation of twins. Among the boundary

misorientations within a deformed microstructure, the extension twins are typically characterized as those with a boundary misorientation angle of ~86° about the $\langle 1\bar{2}10 \rangle$ axis. Fig. 3 shows the band contrast maps of ROIs A and B along with the twin boundaries. While the map for location A shows a small number, that of location B shows a larger fraction of twin boundaries. This confirms that the features in Fig. 2(c) and the orientations

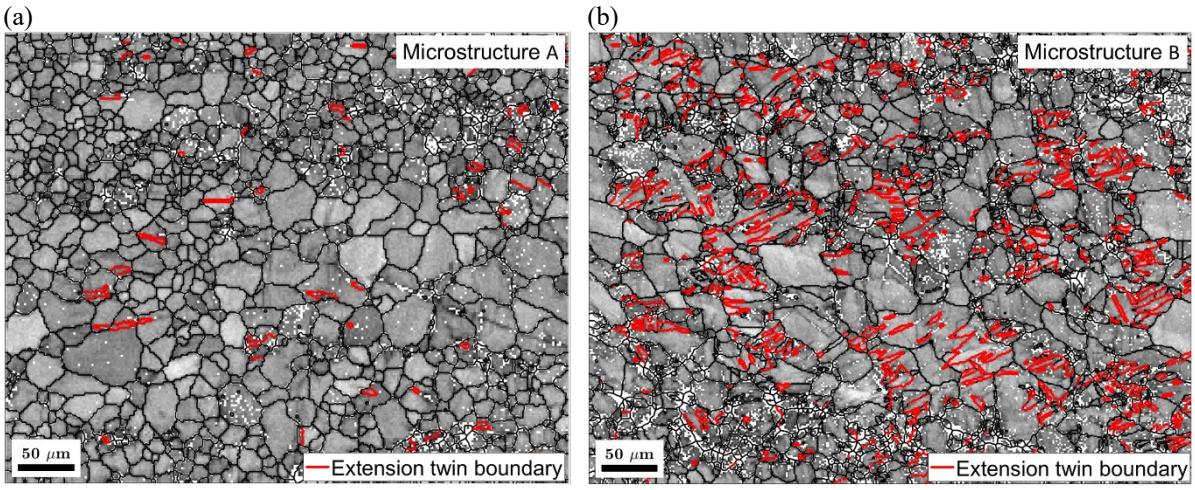

Fig. 3. The band contrast map along with twin boundaries within the deformed microstructure of (a) ROI A and (b) ROI B. This confirms that the observed features in Fig. 2(c) and the orientations in Fig. 2(d) are indeed extension twins. Further, the fraction of twin boundaries is more in ROI B compared to that of ROI A. (For interpretation of the references to colour in this figure legend, the reader is referred to the Web version of this article.)

observed in Fig. 2(d) are indeed extension twins. It is to be noted that this, to the authors' knowledge, is the first study to report the deformed texture observed in Fig. 2(d), which is generated as a result of twinning, in three-point bending of Mg alloys. This shows that the macroscopically applied load is accommodated by different deformation modes within a three-point bending sample. While the deformation appears to be accommodated by crystallographic slip at location A, it is the combination of slip and twinning at B.

It is shown in other studies (e.g. [44]) that the nucleation of twins is sometimes driven by local dislocation structures. In order to understand the distribution of dislocation densities at locations A and B, the Hough-based method [45] is employed to determine GNDs using MTEX. Fig. 4(a) shows the GND distribution for location A, while Fig. 4(b) for that of B.

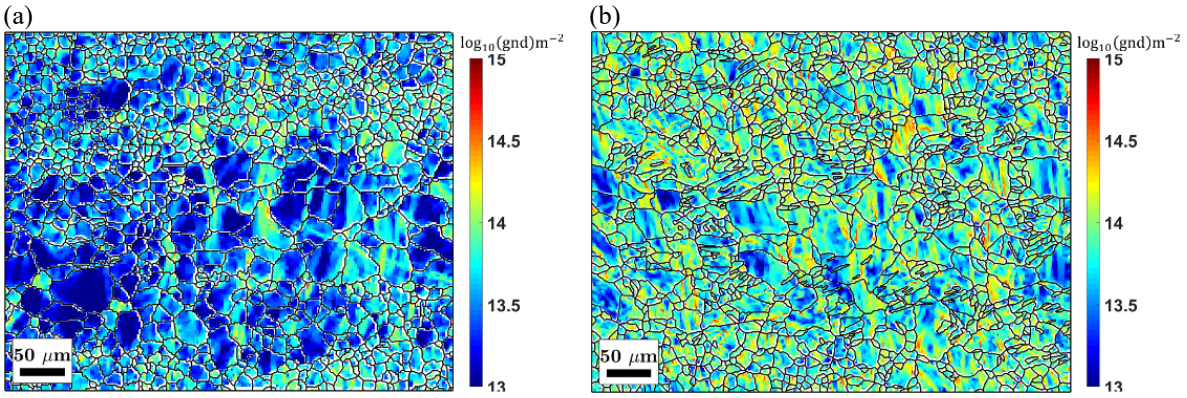

Fig. 4. The distribution of geometrically necessary dislocation (GND) density calculated using Hough-based method within (a) ROI A and (b) ROI B. The GND in ROI B is more than that of A, which could be due to the formation of twins. (For interpretation of the references to colour in this figure legend, the reader is referred to the Web version of this article.)

These figures show profound differences, where the GNDs at A appear to be localized within the fine grains, while that at B are distributed throughout the microstructure. The high GND at location B may have formed before the nucleation of twins. In that case, as the G_{SE} that drives twin nucleation is preferentially stored in the GNDs, the location B, which contains high GNDs, nucleates more twins compared to that of A. However, it is also perfectly feasible that the twin boundaries after nucleation and growth may have acted as barriers causing local strain gradients that led to the development of GNDs. Thus, a detailed analyses of the stress-states at locations A and B are necessary to establish the drivers for twin formation.

3.2 Isotropic elasto-plastic three-point bending analyses

Before attempting to understand the drivers of non-classical twin nucleation and variant selection, it is necessary to establish the nature of stress-states that develop during three-point bending and their relationship with ROIs A and B. Therefore, an isotropic elasto-pastic continuum scale simulation of three-point bending is performed first using ABQUS CAE. Fig. 5(a) shows the simulation set-up, which also indicates the ROIs A and B. The simulation was performed by applying a displacement of 2 mm at the strain rate of 0.001 1/s. An elastic modulus of 44.8 GPa was used. The yield stress and hardening co-efficient were extracted from the experimental data reported in [25].

Fig. 5(b) and (c) show the σ_{XX} and σ_{XY} distributions after three-point bending, where the red dashed line indicates the neutral axis. These stress distributions indicate that the ROI A lies in

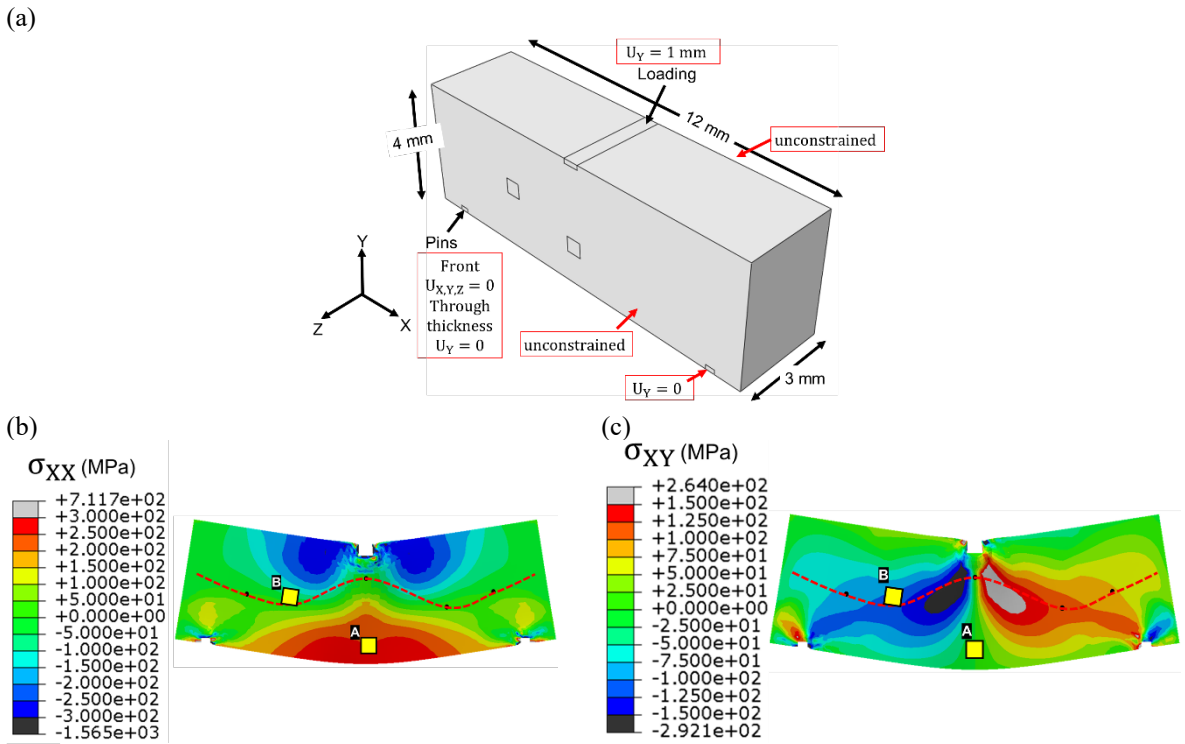

Fig. 5. The isotropic elasto-plastic analyses of three-point bending showing (a) the simulation set-up and (b) the distribution of stress along the X-axis (σ_{XX}) and (c) shear stress (σ_{XY}). The red dashed line indicates the neutral axis. The ROI B is located within the shear region of the sample, while A in tensile region indicating that shear stress state may drive more twin formation. (For interpretation of the references to colour in this figure legend, the reader is referred to the Web version of this article.)

the tensile region, while B in the shear region of the sample. That is, the symmetric deformation bands observed in Fig. 1(c) are formed in the shear region of the sample and the relatively smoother regions correspond to tensile and compressive regions. For the microstructure considered in this study (see Fig. 1(a)), the c-axes of the majority of grains in the tensile region are likely to be in compression (unfavourable for classical twinning), while those in the compressive region in tension (favourable for classical twinning). Further, the ROIs are located such that the corresponding local stress-states can be approximated as uniaxial tensile and simple shear respectively. Therefore, in summary, the preliminary continuum scale modelling shows that the ROI B lies in the shear region of the sample suggesting that shear drives nucleation of more twins compared to that of the tensile stress-state. However, as the nucleation

of twins is a complex phenomenon influenced by several factors, the numerical analyses are developed to investigate local heterogeneity in the microstructure and the drivers of non-classical twin formation

3.3 Crystal plasticity finite element analyses of twin formation and variant selection

The detailed crystal plasticity analyses of the effect of stress-state on twin nucleation requires an explicit representation of the microstructure to account for local heterogeneities. For this, a region of microstructure at ROI B is utilized as shown in Fig. 6(a), where the ROI on the right

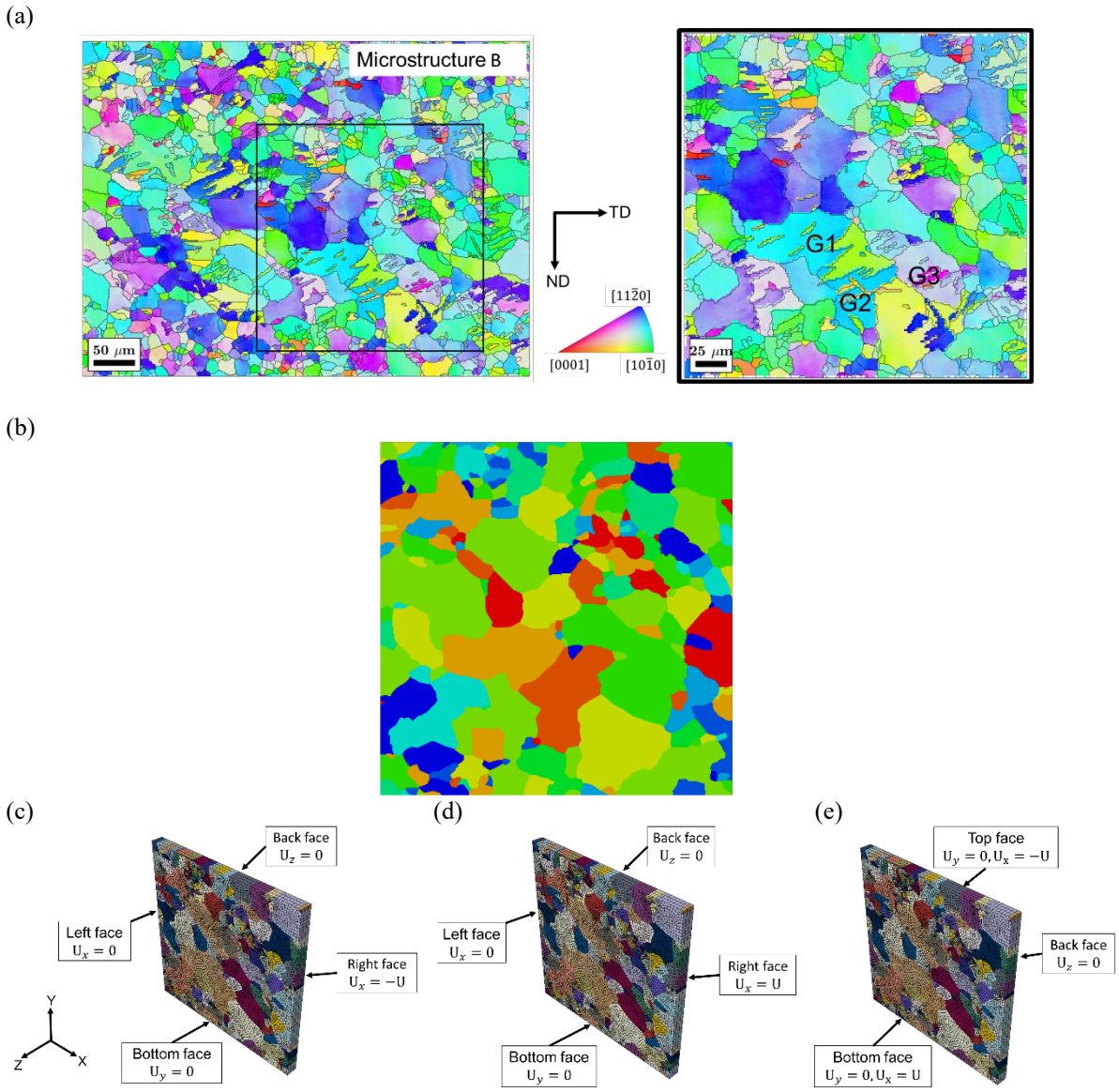

Fig. 6. The simulation set-up for the crystal plasticity analyses showing (a) the ROI and the grains of interest G1, G2 and G3 for the CPFE analyses, (b) the reconstruction of the undeformed microstructure for CPFE analyses, and boundary conditions for (c) uniaxial compression, (d) uniaxial tension and (e) simple shear. The twins are removed from the deformed microstructure in (a) and the average crystallographic orientations of

grains are assumed to be equivalent to the undeformed orientations. (For interpretation of the references to colour in this figure legend, the reader is referred to the Web version of this article.)

244

245 shows that used for crystal plasticity analyses. The figure also indicates three grains of interest
246 (GOIs) G1, G2 and G3, which are considered later for more detailed analyses. In order to
247 replicate the microstructure before deformation, the ROI for CPFE analyses is reconstructed to
248 comprise only the parent grains as shown in Fig. 6(b). The crystallographic orientations within
249 the respective grains of the deformed microstructure are averaged and assumed to be equivalent
250 to the undeformed crystallographic orientations of parent grains used for crystal plasticity
251 analyses. In addition, the local deformation within three-point bending is inhomogeneous,
252 especially in the shear region of the sample. However, based on the distributions in Fig. 5(a)
253 and (b), the stress-states at A and B may be considered approximately to be uniaxial tensile and
254 simple shear respectively thus enabling the investigation of the effect of stress-state on the
255 drivers of non-classical twin formation. In addition to these, as the compressive stress states
256 are likely to drive the formation of classical twins, the uniaxial compression along the X
257 direction is also considered for the sake of completeness, in the context of non-classical twin
258 formation. The boundary conditions to simulate these stress-states are depicted in Fig. 6(c), (d)
259 and (e) respectively. In the case of compression (Fig. 6(c)), the left, bottom and back surfaces
260 are constrained along X, Y and Z directions respectively and the compressive displacement is
261 applied in the X direction on the right face. Similar constraints are applied for tension and the
262 microstructure is loaded in tension along the X direction on the right face. For shear, the bottom
263 face is constrained both along X and Y, the back face constrained along Z and the top face
264 subject to X direction shearing. These cases are all deformed to a macroscopic equivalent
265 plastic strain of 0.15 % (near yield point), in order to assess the effect of stress-state alone on
266 non-classical twin nucleation.

The resulting spatial distributions of G_{SE} developed within the microstructures loaded in compression, tension and shear are shown in Fig. 7(a), (b) and (c) respectively. Note that the legend on the left is limited to a maximum G_{SE} of 0.015 J/m^2, which corresponds to the *critical* G_{SE} required for non-classical twin nucleation in this alloy [30, 17]. The initial assessment shows that the distributions of predicted G_{SE} for compression and tension loading are similar but rather different to that for shear. In addition, the high energy locations are confined only to a

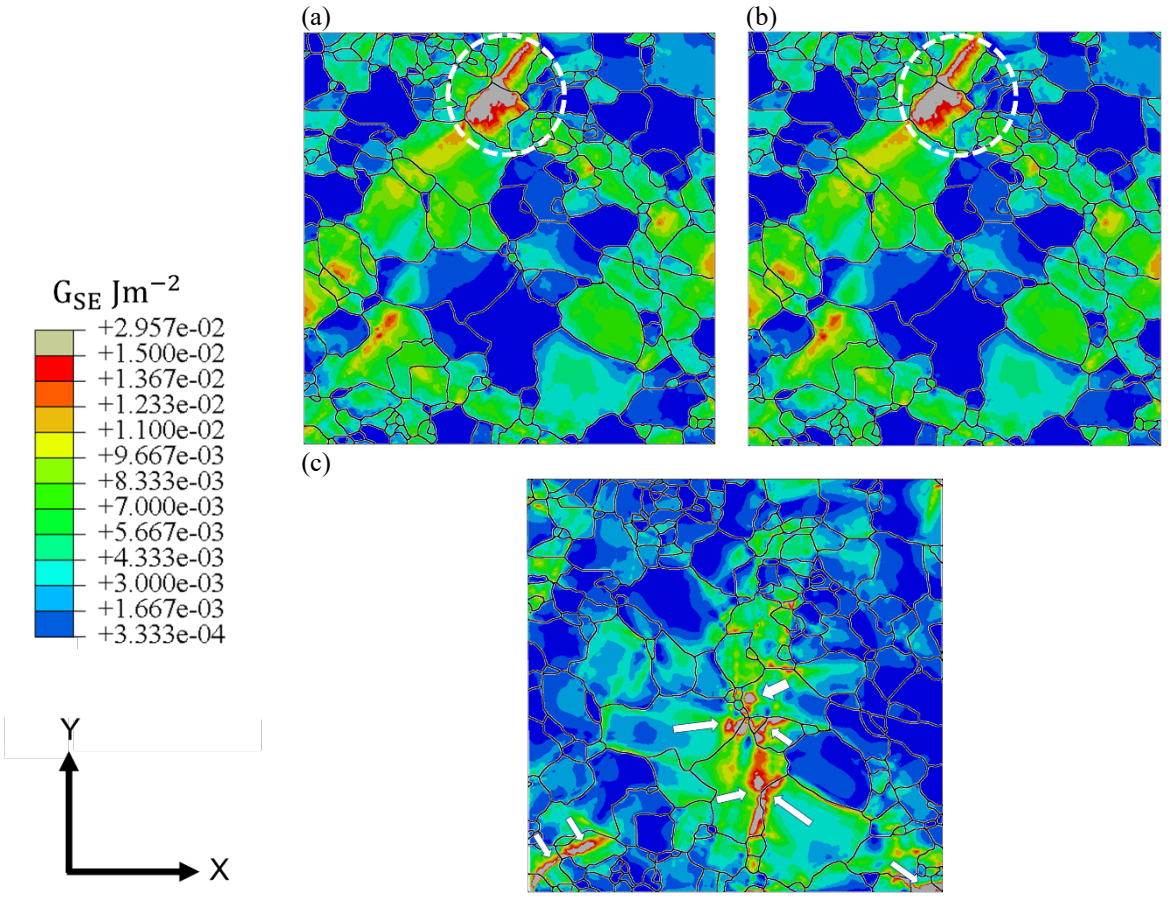

Fig. 7. The distribution of the stored energy density (G_{SE}) at 0.15 % equivalent strain in the deformed microstructure of (a) uniaxial compression along X, (b) uniaxial tension and (c) simple shear. The legend on the left is limited to a maximum G_{SE} of 0.015 J/m2, which corresponds to the critical GSE required for twin nucleation in this alloy. Observe the similarity in G_{SE} distributions within uniaxial tension and compression RVEs, and the distribution of relatively higher G_{SE} within sheared RVEs. The white dashed circles show that the G_{SE} in (a) and (b) are confined to only a couple of grains. In contrast, the G_{SE} within sheared microstructure is distributed within several grains as indicated by the white arrows. (For interpretation of the references to colour in this figure legend, the reader is referred to the Web version of this article.)

couple of grains as indicated by dashed circles in Fig. 7(a) and (b). In contrast, the G_{SE} in shear loading shows a distinct spatial distribution with high energy locations within several grains (highlighted using white arrows in Fig. 7(c)) indicating that the shear stress-state will drive more non-classical twin nucleation compared to that of tension and compression.

While the qualitative analyses seem to indicate that the shear loading nucleates more twins, it is necessary to quantify the nucleation sites in these loading conditions. Therefore, the potential nucleation sites in the deformed microstructures are determined by identifying the number of materials points at the vicinity of grain boundaries that possess G_{SE}>0.015 J/m^2. These materials points are indicative of locations possessing highest probability of twin formation at the vicinity of the grain boundaries (e.g. [46]). The numbers of potential nucleation sites for compression, tension and shear stress-states are shown in Fig. 8(a). Similar to the qualitative analyses, the number of twin nucleation sites in material with shear stress-state are evidently much higher compared to that of compression and tension, with a sequence of tension <

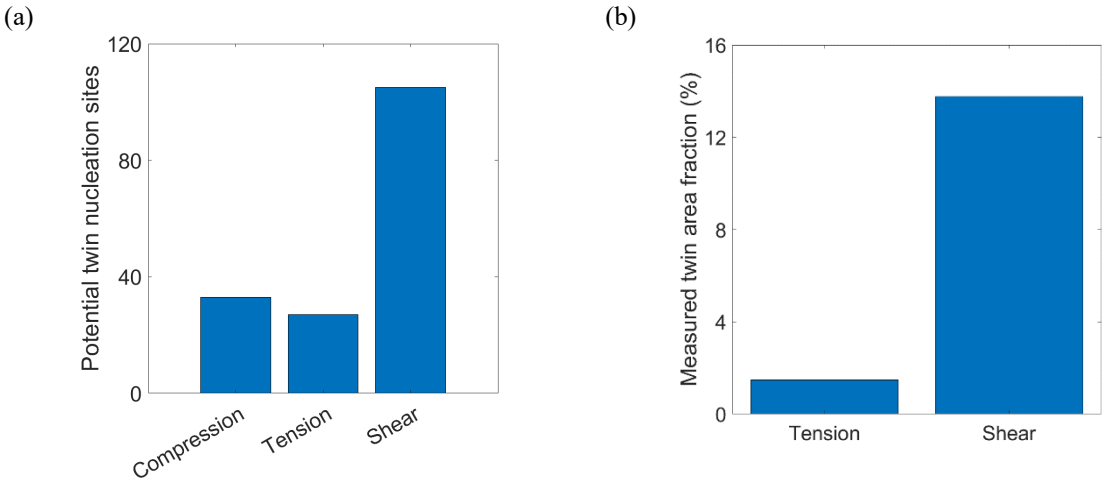

Fig. 8. The comparison between (a) the number of potential nucleation sites at 0.15 % equivalent strain in the microstructure after uniaxial compression, uniaxial tension and simple shear determined using crystal plasticity analyses and (b) the twin area fraction within ROI A (tensile region) and ROI B (shear region) respectively measured from deformed microstructures in Fig. 2(a) and (c). The trends confirm that the shear drives more non-classical twin formation compared to tension and compression stress states. In addition, (a) shows that the compression along X (classical twinning) drives more twinning compared to that of other stress-states, which is consistent with other independent studies.

compression < shear. In order to confirm this further, the area fractions of twins at A (Fig. 2(a)) and B (Fig. 2(c)) are quantified using MTEX. Fig. 8(b) shows the twin area fractions, which follows the trends in Fig. 8(a), and confirms that the area fraction at A (tensile region) is far lower than that of B (shear region). These analyses unequivocally demonstrate the effect of stress-state and that the non-classical twins observed at location B are favoured by local shear stress-states. In addition, for Mg alloy AZ31, the shear activates many more twins than for tensile and compressive stresses, as demonstrated from both crystal plasticity stored energy and experimental observation.

Further, in Fig. 8(a) the stored energy criterion predicts a similar number of potential non-classical twin nucleation sites in compressive and tensile regions, though markedly lower than that for shear. In contrast, other experimental studies reported higher twin volume fractions in compressive compared to the tensile regions of samples (e.g. [7]). However, the investigations in those studies are confined to only classical twins, where the primary mechanistic driver of nucleation is argued to be the TRSS. The formation of twins is a complex phenomenon involving either the storage of sufficient energy to drive non-classical twin nucleation, and shear energy determining variant selection or, for classical twins, the development of sufficient favourable local stresses and hence TRSSs.

In order to further explore the mechanistic preference for non-classical twin formation under states of shear stress, detailed local microstructural analyses, and the spatial distributions of G_{SE} in shear loading within the GOIs (shown in Fig. 6(a)) are investigated to validate (or otherwise) against experimental observations. The Fig. 9(i)s show the spatial distribution of G_{SE} within G1, G2 and G3 along with the path AB used to quantify the G_{SE}. In these figures, the black solid line indicates the grain boundaries, while the grey lines show twin boundaries. The distributions of G_{SE} along the paths are depicted in the Fig. 9(ii)s for all the GOIs. During deformation, the twins nucleate, propagate and grow to accommodate the local stress/strain

incompatibilities. While a nucleated twin propagates and grows, the stress-relaxation caused by this twin and the evolution of local deformation with applied load may

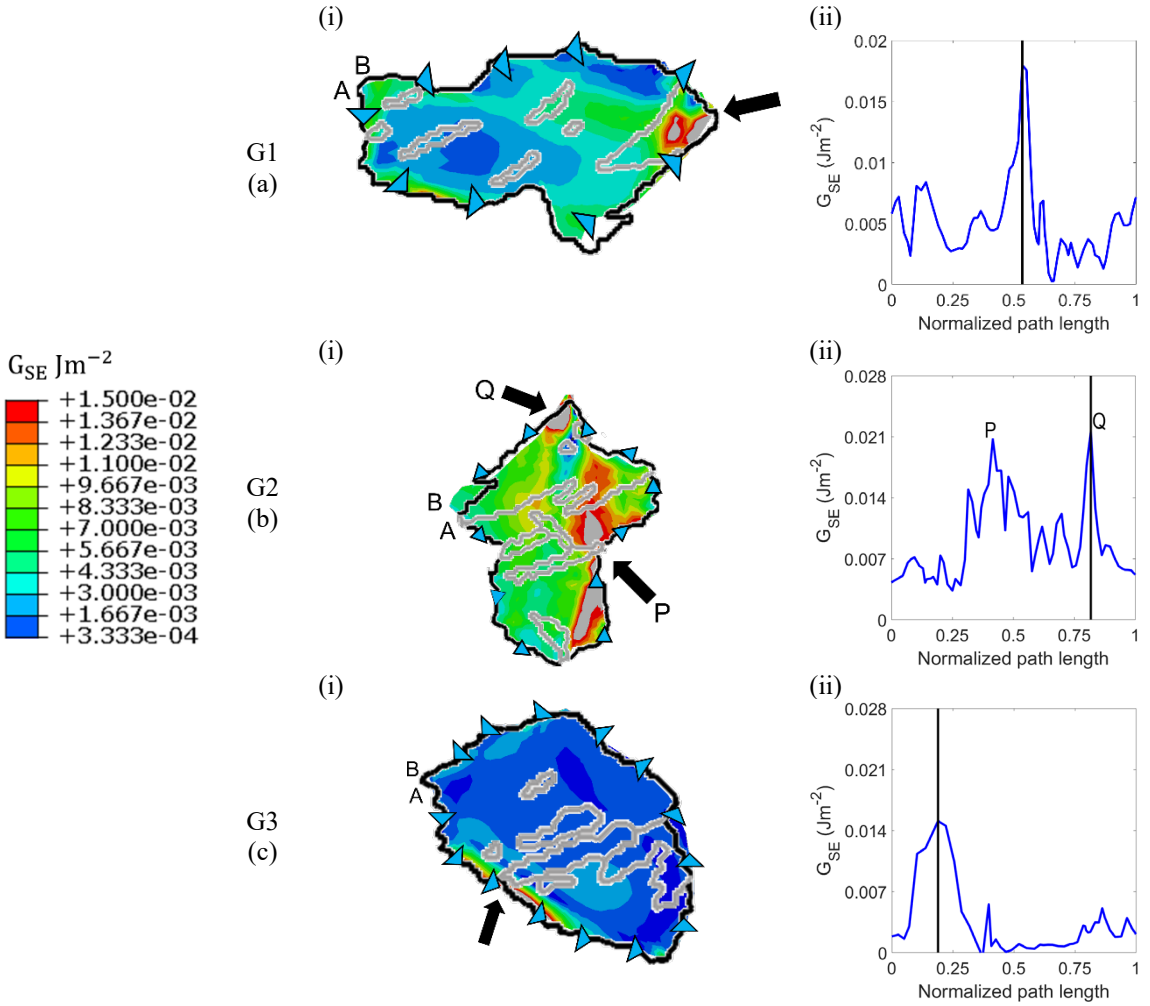

Fig. 9. The stored energy density within the grains of interest in microstructure subjected to simple shear (a) G1, (b) G2 and (c) G3, where (i) show the spatial distribution within the grains and (ii) the distribution along respective paths. The black and grey solid lines in (i) indicate the parent grain and twin boundaries extracted from experimental microstructures. The black solid lines in (ii) indicate the location where the twin tips intersect with the parent grain boundaries. (For interpretation of the references to colour in this figure legend, the reader is referred to the Web version of this article.)

nucleate more twins within the parent grain. This implies that the parent grain contains twins with different volumes and the twin that nucleated first is likely to possess the highest volume. Thus, the G_{SE} analyses within the GOIs are restricted only to twins with highest volume, which is reflected by their area fractions. Further, it is to be noted that the sample is loaded until a displacement of 2 mm in the current study. This means that the twins may have nucleated and grown to a considerable size rendering it impossible to locate the intersection of twin tips with

parent grain boundaries, which are the highly probable locations of nucleation. In such cases, the local G_{SE} at the vicinity of the twins of interest can be used to identify their nucleation sites [30, 17].

In G1, the twin indicated with black arrow in Fig. 9(i)(a) possesses highest area fraction and is likely to have nucleated at 0.15 % strain. The qualitative observation shows a hot spot at the location of the twin of interest (TOI). This hotspot location is represented as a black vertical line in Fig. 9(ii)(a) that shows G_{SE} distribution along path AB. It is clearly evident from the figure that the G_{SE} at that location exceeds the *critical* value, which drives the nucleation of the TOI. Similarly, the hotspots in G_{SE} distribution within G2 are indicated as P and Q in Fig. 9(i)(b). The twin at location Q possesses highest area fraction compared to that of P. The corresponding path-measurement in Fig. 9(ii)(b) shows that the G_{SE} at both locations P and Q exceed the *critical* value suggesting equal probability of twin formation. In the case of G3, Fig. 7(c) shows the local G_{SE} is less than the *critical* value at 0.15 % strain. Thus, this grain may have nucleated twins at slightly higher strain. Therefore, the distribution of G_{SE} within G3 is analysed at 0.4 % strain, which corresponds to that required by the grain to accumulate the *critical* G_{SE}. In G3, the TOI lies at the vicinity of the G_{SE} hotspot indicated with the black arrow in Fig. 9(i)(c). The corresponding distribution along the path corroborates the G_{SE} exceeding the *critical* value that nucleated the twin at 0.4 % strain. Thus, while the G_{SE} satisfactorily predicted the nucleation of twins in G1 and G3, there was ambiguity in the case of G2 (between P and Q), which is hence revisited later for detailed investigation.

Now that the twin nucleation sites are established (except for G2) it is necessary to identify the twin variants to predict variant selection. Several approaches such as the trace and orientation methods are employed to identify the variant selected by the parent grain (e.g. [47, 48, 49]). The former is suitable mainly for twins at lower strains, which allow precise identification of twinning plane [17]. In contrast, the latter is employed irrespective of the deformation level as

the deviation in crystallographic orientation due to plasticity within a twin does not influence the variant selection analyses. Therefore, the orientation method is employed in the current study. Briefly, in the orientation method, the theoretical crystallographic orientations of the all the twin variants are calculated using the approach outlined in [50]. These orientations are compared against the experimental ones to identify the twin variant selected by the parent grain. Fig. 10 shows the basal pole figures containing discrete orientations of GOI measured

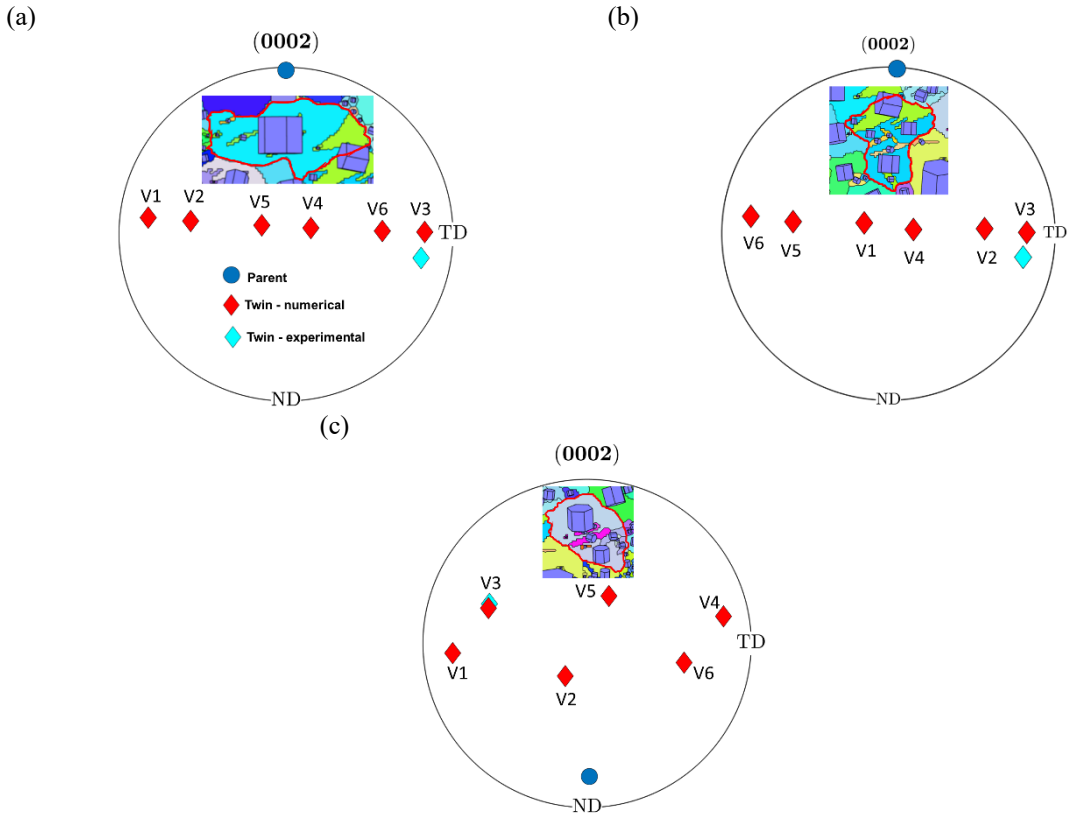

Fig. 10. The basal pole figures showing the grains of interest and the respective twins, and the numerical (red diamonds) and experimental (cyan diamond) crystallographic orientations of twins in (a) G1, (b) G2 and (c) G3, where V# indicates the variant (V) of type #. This analysis shows that the variant 3 is selected in all the grains. (For interpretation of the references to colour in this figure legend, the reader is referred to the Web version of this article.)

experimentally and of twin variants that are calculated (red diamond) and measured in experiments (cyan diamond). In addition, these pole figures also show the GOIs along with their crystallographic orientations indicated using HCP unit cells. The order V1-V6 in the nomenclature of twin variants in Fig. 10 follows that listed in Paramatmuni et al [30]. The comparison between the calculated and measured orientations shows that the variant three is

selected by all the GOIs. In addition, it appears from Fig. 10 that the c-axes of the GOIs are oriented near-parallel to the ND suggesting that the respective twins are non-classical in nature, which are mainly driven by the local energy and defect sources. This can be confirmed by studying the spatial distribution of the TRSS for variant 3 within the GOIs as shown in Fig. 11. It is worth recalling

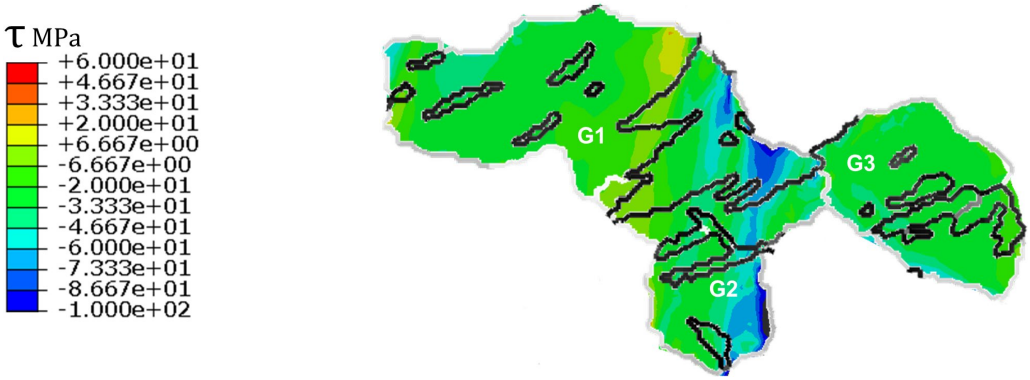

Fig. 11. The spatial distribution of the TRSS for variant 3 within the grains of interest for simple shear loading condition at 0.15% equivalent strain. The black lines indicate twin boundaries adapted from the experimental microstructures. The TRSS is largely negative within the GOIs indicating that the twin formation is not driven by local stresses. (For interpretation of the references to colour in this figure legend, the reader is referred to the Web version of this article.)

here that the twins are unidirectional, which implies that the associated TRSS should always be positive for stress driven twin nucleation. However, the distribution in Fig. 11 clearly shows negative TRSS confirming that the twins within the GOIs are driven by local energy and defect sources.

The S_{SE}, which is demonstrated in [30] as a robust and reliable criterion for non-classical twins, is now employed to predict variant selection. According to this criterion, the twin variant with the least S_{SE} at the *critical* G_{SE} location is selected by the parent grain. The distribution of S_{SE} along the paths AB in Fig. 9(i) for the GOIs is shown in Fig. 12, where the vertical lines indicate the locations of interest. In the case of G1 (Fig. 12(a)), the variants 1, 2, 4 and 5 contain higher but similar S_{SE}. In contrast, the S_{SE} for variants 3 and 6 are least and close to zero. While this seem to suggest that the variants 3 and 6 are equally probable, it is perfectly feasible that the

heterogeneity caused by microstructure in the subsurface of the sample facilitated the selection of variant 3. In addition, as the twinning is a three-dimensional defect, the least S_{SE} in the subsurface at the vicinity of the *critical* G_{SE} may have nucleated variant 3 in G1.

The S_{SE} distribution for G2 is shown in Fig. 12(b). The G_{SE} predicted two equally probable nucleation sites, P and Q, at 0.15 % strain in Fig. 9(ii)(b). This causes ambiguity as the twin at location Q possesses higher area fraction than that of P. The distribution at P and Q clearly shows that the S_{SE} at location P is higher for all the twin variants compared to that of Q. As

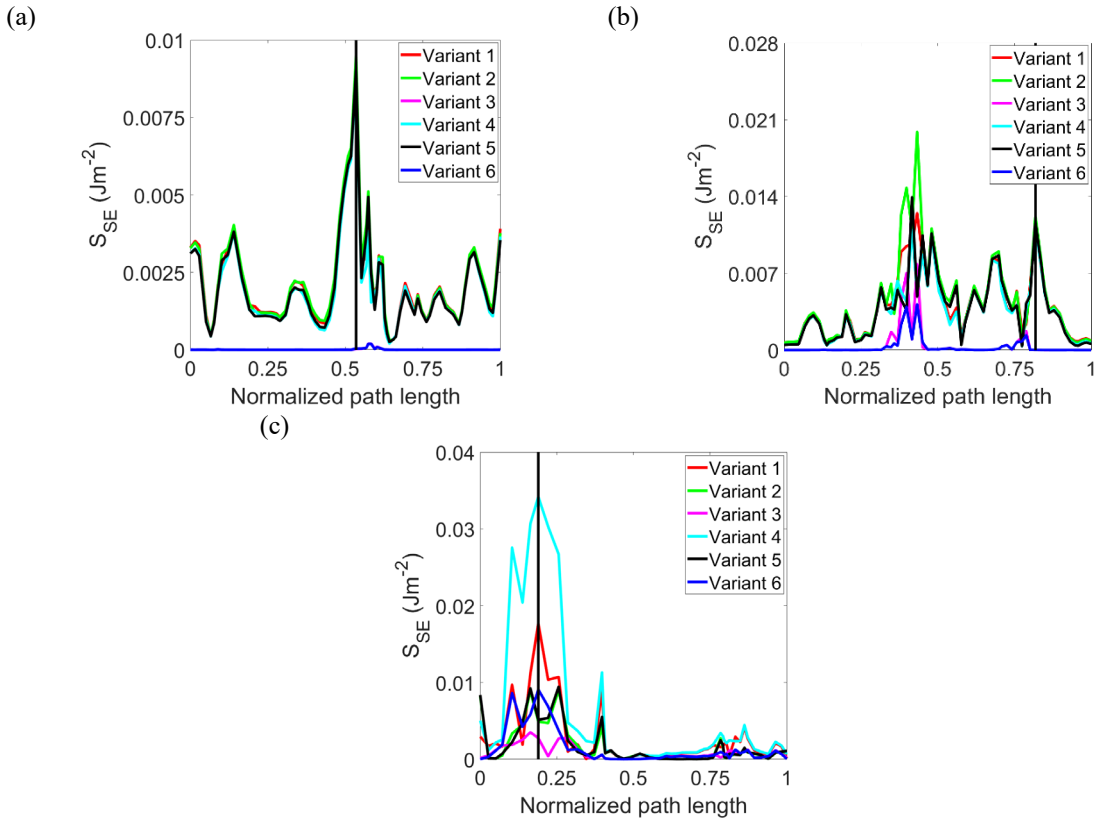

Fig. 12. The distribution of the shear stored energy density (S_{SE}) density along the paths shown in Fig. 9 for all the six twin variants within the grains of interest (a) G1, (b) G2 and (c) G3. The black solid line indicates the location of high G_{SE}, where twins nucleate. Recall that variant 3 is the experimentally determined active twin variant in these grains. According to the S_{SE} criterion, the twin variant with least S_{SE} is selected by the parent grain. The S_{SE} is the least for variant 3 in G3, while it is zero for variants 3 and 6 in G1 and G2. The shear stored energy density satisfactorily predicts the variant selection in these grains. (For interpretation of the references to colour in this figure legend, the reader is referred to the Web version of this article.)

reported in [30], in the case of non-classical twins, the location within the parent grain with maximum G_{SE} and minimum S_{SE} is preferentially chosen by the parent grain to nucleate twins.

Therefore, the twin is nucleated at location Q in G2, which satisfies these criteria. Once the twin is nucleated at Q, the local stress redistribution caused by the nucleation relaxes the G_{SE} within G2. At location Q, similar to G1, the variants 1, 2, 4 and 5 possess highest S_{SE} compared to variants 3 and 6, which are close to zero. However, as in case of G1, the local S_{SE} heterogeneities caused by the microstructure in sample subsurface may have driven the selection of variant 3. Finally, Fig. 12(c) shows the S_{SE} distribution for G3. Here, the S_{SE} of variant 3 is the least at the location of interest, which is, therefore, selected by the parent grain as shown in Fig. 10(c).

4. Discussion

In this study, the effect of stress-state on twin nucleation is investigated by subjecting the rolled Mg alloy AZ31 to three-point bending (Fig. 1). The strong basal texture of the sample allows detailed investigation of the effect of stress-state as the variation in crystallographic orientations of grains within the sample is minimum. The sample is loaded such that the bending stress is normal to the c-axes of the grains (ND). As mentioned earlier in section 1, to the authors' knowledge, [16] and [15] are the only studies in the literature that performed bending with similar loading conditions. This bending condition causes the development of three main stress-states - tensile, compressive and shear - across the sample surface (Fig. 5). The analyses of microstructures within the tension and shear regions (Fig. 2) show a distinct difference in the deformed textures developed (due to twinning), which, to the authors' knowledge, has not been reported in the literature. It is confirmed using the grain boundary misorientation angle (Fig. 3) that the observed deformed texture within the shear region is caused by the formation of extension twins.

The deformed microstructures and the formation of twins reported in this study are similar to that in [16], which reported the microstructures at the tensile and apparently near-shear regions. Similarly, the qualitative assessment of microstructures in [20] also suggest that the regions

412 with local shear deformation state drive more twin formation. The formation of twins in tensile
413 and shear regions is quantified by measuring the twin area fraction shown in Fig. 8(b). These
414 area fractions are comparable with that quantified in [15], which reported least twin volume
415 fraction in the tensile regions of three-point bending sample loaded along ND. Further, the
416 detailed numerical analyses show that the shear drives more twin nucleation compared to that
417 of tensile and compressive stress-states, and that the G_{SE} and S_{SE} accurately predict the twin
418 nucleation and variant selection.

419 It is shown in Fig. 12 that the S_{SE} satisfactorily predicts the variant selection for G3 but shows
420 dependency on the subsurface of the sample for G1 and G2. While it is perfectly feasible that
421 the S_{SE} is minimum for variant 3 in the subsurface at the vicinity of the *critical* G_{SE}, it is
422 necessary to validate the fidelity of the S_{SE} criterion. It is argued in other studies that the growth
423 of a twin interface follows the path of least energy [51, 52, 53]. This means that if variant 3
424 were to nucleate in the subsurface at the vicinity of *critical* G_{SE} and grow to the free surface of
425 the sample, the locations of interest within G1 and G2 should possess least energy irrespective
426 of the deformation level to accommodate the twin interface. In order to confirm that the S_{SE} is
427 minimum at the locations of interest to facilitate twin growth, the distribution of S_{SE} for all the
428 twin variants of G1 and G2 is studied at higher strain levels, which may render non-zero S_{SE}
429 for variant 3. Fig. 13 shows the distribution of S_{SE} along paths AB (Fig. 9(i)) for G1 and G2 at
430 0.9 % strain. This figure clearly shows that the S_{SE} for variant 3 is the least for both G1 and
431 G2. This minimum S_{SE} within G1 and G2 at higher strain levels confirms that the identified
432 locations of interest indeed promote the formation of variant 3 and that the S_{SE} accurately
433 predicts the variant selection.

434

435

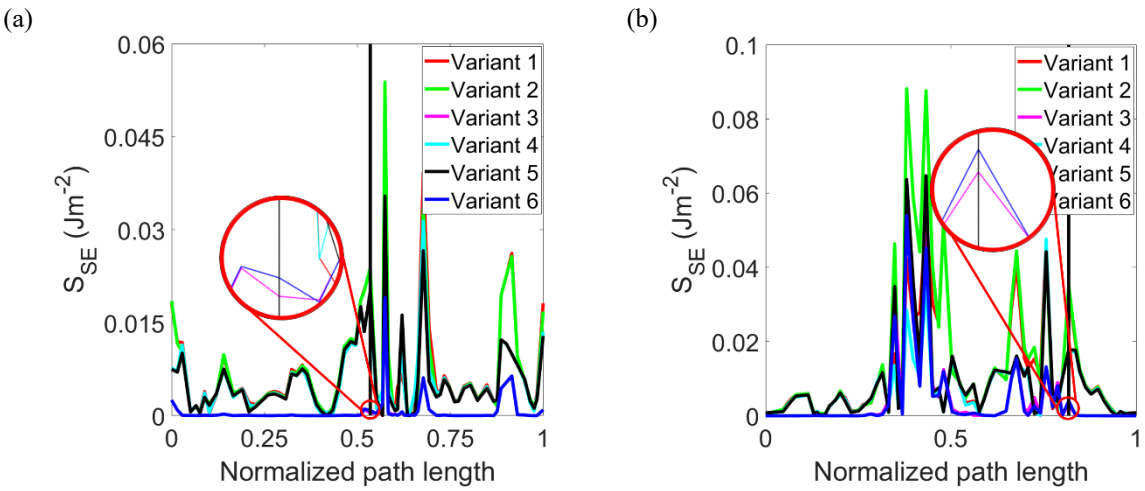

Fig. 13. The distribution of the shear stored energy (S_{SE}) density along the paths shown in Fig. 9 for (a) G1 and (b) G2 at 0.9 % strain. The black solid line indicates high G_{SE}, where twins nucleate. The S_{SE} of variant 3 is the least for both the grains confirming that the locations of interest are the path of least energy that accommodate the twin interface. (For interpretation of the references to colour in this figure legend, the reader is referred to the Web version of this article.)

5. Conclusions

The effect of stress state on twinning at near-yield point is investigated by performing three-point bending of rolled Mg alloy AZ31. While three-point bending generates bending (normal to ND in this study) and shear stresses, the presence of strong texture reduces uncertainty caused by the crystallographic orientations of parent grains and allows detailed study of the effect of stress-states. The experimental observations, both texture and microstructure, show the presence of non-classical twins predominantly in the shear compared to the tensile or compressive regions of the deformed sample. These observations are reinforced with strain-gradient crystal plasticity analyses which corroborate that the shear drives higher stored energy densities which nucleate more twins at yield point compared to the bulk tensile and compressive stress-states. The stored energy criterion, validated against experimental observations, captures the experimental twin nucleation sites, while the shear stored energy density allows precise prediction of variant selection.

Acknowledgements

CP acknowledges the award of Imperial College President's generous PhD scholarship. CP is also thankful to Mr. Rohan, Dr. Vasilis Karamitros and Dr. Bo Chen for assistance in modelling and experiments. FPED acknowledges his Royal Academy of Engineering/Rolls-Royce research chair funding.

References

[1] J. Weiler, A review of magnesium die-castings for closure applications, Journal of Magnesium and Alloys 7 (2) (2019) 297–304.

[2] F.-K. Chen, T.-B. Huang, Formability of stamping magnesium-alloy az31 sheets, Journal of Materials Processing Technology 142 (3) (2003) 643–647.

[3] S. Yoshihara, H. Nishimura, H. Yamamoto, K.-i. Manabe, Formability enhancement in magnesium alloy stamping using a local heating and cooling technique: circular cup deep drawing process, Journal of Materials Processing Technology 142 (3) (2003) 609–613.

[4] W. Wang, L. Huang, K. Tao, S. Chen, X. Wei, Formability and numerical simulation of az31b magnesium alloy sheet in warm stamping process, Materials & Design 87 (2015) 835–844.

[5] L. Zhang, G. Huang, H. Zhang, B. Song, Cold stamping formability of az31b magnesium alloy sheet undergoing repeated unidirectional bending process, Journal of Materials Processing Technology 211 (4) (2011) 644–649.

[6] M. Gao, Q. Wang, L. Li, Z. Ma, Energy-economizing optimization of magnesium alloy hot stamping process, Processes 8 (2) (2020) 186.

[7] S. Härtel, M. Graf, T. Lehmann, M. Ullmann, Influence of tension-compression anomaly during bending of magnesium alloy az31, Materials Science and Engineering: A 705 (2017) 62–71.

[8] G. M. Lee, J. U. Lee, S. H. Park, Effects of surface roughness on bending properties of rolled az31 alloy, Journal of Magnesium and Alloys.

[9] B. Jeon, M.-S. Kim, S.-H. Choi, Y. Jeong, Finite element analysis using elasto-visco-plastic self-consistent polycrystal model for e-form mg sheet subjected to bending, Journal of Magnesium and Alloys.

[10] G. Huang, L. Wang, H. Zhang, Y. Wang, Z. Shi, F. Pan, Evolution of neutral layer and microstructure of az31b magnesium alloy sheet during bending, Materials Letters 98 (2013) 47–50.

[11] W. Ren, J. Li, R. Xin, Texture dependent shifting behavior of neutral layer in bending of magnesium alloys, Scripta Materialia 170 (2019) 6–10.

[12] L. Jin, J. Dong, J. Sun, A. A. Luo, In-situ investigation on the microstructure evolution and plasticity of two magnesium alloys during three-point bending, International Journal of Plasticity 72 (2015) 218–232.

[13] Y. Paudel, J. Indeck, K. Hazeli, M. W. Priddy, K. Inal, H. Rhee, C. D. Barrett, W. R. Whittington, K. R. Limmer, H. El Kadiri, Characterization and modeling of {101 2} twin banding in magnesium, Acta Materialia 183 (2020) 438–451.

[14] W. Wang, W. Zhang, W. Chen, G. Cui, E. Wang, Effect of initial texture on the bending behavior, microstructure and texture evolution of zk60 magnesium alloy during the bending process, Journal of Alloys and Compounds 737 (2018) 505–514.

[15] D. Tang, K. Zhou, W. Tang, P. Wu, H. Wang, On the inhomogeneous deformation behavior of magnesium alloy beam subjected to bending, International Journal of Plasticity 150 (2022) 103180.

[16] D. Liu, R. Xin, Z. Li, Z. Liu, X. Zheng, Q. Liu, The activation of twinning and texture evolution during bending of friction stir welded magnesium alloys, Materials Science and Engineering: A 646 (2015) 145–153.

[17] C. Paramatmuni, Y. Guo, P. J. Withers, F. P. Dunne, A three-dimensional mechanistic study of the drivers of classical twin nucleation and variant selection in mg alloys: A mesoscale modelling and experimental study, International Journal of Plasticity 143 (2021) 103027.

[18] J. Baird, B. Li, S. Y. Parast, S. Horstemeyer, L. Hector Jr, P. Wang, M. Horstemeyer, Localized twin bands in sheet bending of a magnesium alloy, Scripta Materialia 67 (5) (2012) 471–474.

[19] Z. McClelland, B. Li, S. Horstemeyer, S. Brauer, A. Adedoyin, L. Hector Jr, M. Horstemeyer, Geometrically necessary twins in bending of a magnesium alloy, Materials Science and Engineering: A 645 (2015) 298–305.

[20] H. Huang, A. Godfrey, J. Zheng, W. Liu, Influence of local strain on twinning behavior during compression of az31 magnesium alloy, Materials Science and Engineering: A 640 (2015) 330–337.

[21] B. Song, N. Guo, T. Liu, Q. Yang, Improvement of formability and mechanical properties of magnesium alloys via pre-twinning: A review, Materials & Design (1980-2015) 62 (2014) 352–360.

[22] H. Watanabe, Y. Sasakura, N. Ikeo, T. Mukai, Effect of deformation twins on damping capacity in extruded pure magnesium, Journal of Alloys and Compounds 626 (2015) 60–64.

[23] J. U. Lee, Y. J. Kim, S.-H. Kim, J. H. Lee, M.-S. Kim, S.-H. Choi, B. G. Moon, Y. M. Kim, S. H. Park, Texture tailoring and bendability improvement of rolled az31

alloy using {10–12} twinning: The effect of precompression levels, Journal of Magnesium and Alloys 7 (4) (2019) 648–660.

[24] J. Deng, J. Tian, Y. Zhou, Y. Chang, W. Liang, J. Ma, Enhanced formability of magnesium alloy rolled plates by 10 1 2 tensile twinning and recrystallization, Materials 15 (18) (2022) 6253.

[25] C. Paramatmuni, F. P. Dunne, Effect of twin crystallographic orientation on deformation and growth in mg alloy az31, International Journal of Plasticity 135 (2020) 102775.

[26] B. Chen, J. Jiang, F. P. Dunne, Microstructurally-sensitive fatigue crack nucleation in ni-based single and oligo crystals, Journal of the Mechanics and Physics of Solids 106 (2017) 15–33.

[27] F. Bachmann, R. Hielscher, H. Schaeben, Texture analysis with mtex–free and open source software toolbox, in: Solid State Phenomena, Vol. 160, Trans Tech Publ, 2010, pp. 63–68.

[28] F. Bachmann, R. Hielscher, H. Schaeben, Grain detection from 2d and 3d ebsd dataâ€”specification of the mtex algorithm, Ultramicroscopy 111 (12) (2011) 1720–1733.

[29] F. Dunne, D. Rugg, A. Walker, Lengthscale-dependent, elastically anisotropic, physically-based hcp crystal plasticity: application to cold-dwell fatigue in ti alloys, International Journal of Plasticity 23 (6) (2007) 1061–1083.

[30] C. Paramatmuni, Z. Zheng, W. M. Rainforth, F. P. Dunne, Twin nucleation and variant selection in mg alloys: An integrated crystal plasticity modelling and experimental approach, International Journal of Plasticity 135 (2020) 102778.

[31] G. I. Taylor, The mechanism of plastic deformation of crystals. part i.â€”theoretical, Proceedings of the Royal Society of London. Series A, Containing Papers of a Mathematical and Physical Character 145 (855) (1934) 362–387.

[32] J. Nye, Some geometrical relations in dislocated crystals, Acta metallurgica 1 (2) (1953) 153–162.

[33] A. Arsenlis, D. Parks, Crystallographic aspects of geometrically-necessary and statistically-stored dislocation density, Acta materialia 47 (5) (1999) 1597–1611.

[34] J. Cheng, S. Ghosh, A crystal plasticity fe model for deformation with twin nucleation in magnesium alloys, International Journal of Plasticity 67 (2015) 148–170.

[35] J. Jeong, M. Alfreider, R. Konetschnik, D. Kiener, S. H. Oh, In-situ tem observation of {101 2} twin-dominated deformation of mg pillars: Twinning mechanism, size effects and rate dependency, Acta Materialia 158 (2018) 407–421.

[36] Z. Zheng, N. G. Prastiti, D. S. Balint, F. P. Dunne, The dislocation configurational energy density in discrete dislocation plasticity, Journal of the Mechanics and Physics of Solids 129 (2019) 39–60.

[37] P. G. Partridge, The crystallography and deformation modes of hexagonal close-packed metals, Metallurgical reviews 12 (1) (1967) 169–194.

[38] J. G. Sevillano, Geometrically necessary twins and their associated size effects, Scripta Materialia 59 (2) (2008) 135–138.

[39] K. D. Molodov, T. Al-Samman, D. A. Molodov, G. Gottstein, On the role of anomalous twinning in the plasticity of magnesium, Acta Materialia 103 (2016) 711–723.

563 [40] V. Livescu, I. J. Beyerlein, C. A. Bronkhorst, O. F. Dippo, B. G. Ndefru,
564 L. Capolungo, H. M. Mourad, Microstructure insensitive twinning: A statistical analysis of
565 incipient twins in high-purity titanium, Materialia 6 (2019) 100303.

566 [41] L. Capolungo, I. Beyerlein, Nucleation and stability of twins in hcp
567 metals, Physical review B 78 (2) (2008) 024117.

568 [42] D. Tromans, Elastic anisotropy of hcp metal crystals and polycrystals, Int.
569 J. Res. Rev. Appl. Sci 6 (4) (2011) 462–483.

570 [43] C. Paramatmuni, A. K. Kanjarla, A crystal plasticity fft based study of
571 deformation twinning, anisotropy and micromechanics in hcp materials: Application to az31
572 alloy, International Journal of Plasticity 113 (2019) 269 – 290.

573 [44] A. Khosravani, D. Fullwood, B. Adams, T. Rampton, M. Miles,
574 R. Mishra, Nucleation and propagation of twins in az31 magnesium alloy, Acta Materialia 100
575 (2015) 202–214.

576 [45] W. Pantleon, Resolving the geometrically necessary dislocation content
577 by conventional electron backscattering diffraction, Scripta Materialia 58 (11) (2008) 994–997.

578 [46] J. Wang, I. Beyerlein, C. Tomé, An atomic and probabilistic perspective
579 on twin nucleation in mg, Scripta Materialia 63 (7) (2010) 741–746.

580 [47] J. Jiang, A. Godfrey, W. Liu, Q. Liu, Microtexture evolution via
581 deformation twinning and slip during compression of magnesium alloy az31, Materials Science
582 and Engineering: A 483 (2008) 576–579.

583 [48] J. J. Jonas, S. Mu, T. Al-Samman, G. Gottstein, L. Jiang, E. Martin, The
584 role of strain accommodation during the variant selection of primary twins in magnesium, Acta
585 Materialia 59 (5) (2011) 2046–2056.

586 [49] Y. Pei, A. Godfrey, J. Jiang, Y. Zhang, W. Liu, Q. Liu, Extension twin
587 variant selection during uniaxial compression of a magnesium alloy, Materials Science and
588 Engineering: A 550 (2012) 138–145.

589 [50] M. Niewczas, Lattice correspondence during twinning in hexagonal
590 close-packed crystals, Acta Materialia 58 (17) (2010) 5848–5857.

591 [51] R. Y. Zhang, M. R. Daymond, R. A. Holt, A finite element model of
592 deformation twinning in zirconium, Materials Science and Engineering: A 473 (1) (2008) 139–
593 146.

594 [52] L. Leclercq, L. Capolungo, D. Rodney, Atomic-scale comparison
595 between twin growth mechanisms in magnesium, Materials Research Letters 2 (3) (2014) 152–
596 159.

597 [53] F. Siska, L. Stratil, J. Cizek, A. Ghaderi, M. Barnett, Numerical analysis
598 of twin thickening process in magnesium alloys, Acta Materialia 124 (2017) 9–16.

599